IR and Metasurface based mm-Wave Camera

Lundgren, Johan; Gustafsson, Mats; Sjöberg, Daniel; Nilsson, Martin

IR and Metasurface based mm-Wave Camera

Johan Lundgren, Mats Gustafsson, Daniel Sjöberg, and Martin Nilsson

Johan Lundgren, johan.lundgren@eit.lth.se
Mats Gustafsson, mats.gustafsson@eit.lth.se
Daniel Sjöberg, daniel.sjoberg@eit.lth.se
Martin Nilsson, martin.nilsson@eit.lth.se

Department of Electrical and Information Technology
Electromagnetic Theory
Lund University
P.O. Box 118
SE-221 00 Lund
Sweden

Abstract

We have developed a technique to measure low-power electromagnetic fields from mm-wave devices non-intrusively by combining a metasurface, designed to absorb power and focus the radiated power in a thermally isolated region, with an infrared camera. The metasurface consists of thermally isolated elements of low mass and highly emissive material for maximal IR conversion of the incident wave. The IR camera captures the converted energy and indirectly images the incident electromagnetic field on the metasurface. The setup combines multi-scale, multi-physical processes to conduct measurements of the incident electromagnetic fields in real time. In this work, the technique is presented and discussed. Measurements are carried out to demonstrate the technique and image the electromagnetic field of a radiating device. The results compare well with simulations and the technique can measure the low power density levels of consumer devices, as well as provide a general visualization of electromagnetic fields in a live setting.

1   Introduction

All around us, there is electromagnetic radiation, whether it is visible light, infrared, ultraviolet, or man-made signals from Wi-Fi and cellular devices. The electromagnetic spectrum is wide and humans, by nature, only detect a small fraction of it, either directly through our eyes or indirectly such as feeling warm from the infrared light near an outdoor lamp or getting tanned by the ultraviolet rays from the sun. Radiation exists even though we do not always see it and is difficult to sense.

As things radiate, and objects interact with radiation, energy will be absorbed and scattered. The absorbed electromagnetic energy gets converted to heat through the movement of electrons [15]. The heat will give rise to infrared photons. These photons can be detected at a different position, giving information on the temperature of the object. By capturing the photons with, for instance, an infrared (IR) camera, it is possible to image the electromagnetic field [3, 6, 11, 16, 17, 20, 22].

This chain of events incorporates many physical phenomena, electromagnetic and thermal, and it is important to consider them all. By doing this we construct a sensor for electromagnetic radiation over large surfaces for radiation otherwise invisible. This is a camera, of sorts, for man-made mm-Waves.

For the idea to work, energy from the electromagnetic field must be absorbed and give a detectable temperature increase, even for low power levels seen in consumer devices. The temperature increase is the signal corresponding to the squared field intensity, and should be strong. For a given absorbed energy, the temperature change can be increased by reducing the mass of the sensor and/or focusing the energy to a smaller sub-region. The strength of the signal can be maintained if these warmer regions can be thermally isolated. The heated subregions can each be viewed as measurement points of the field. For devices in the mm-wave regime these measurement points are given on a cm-scale rather than a pre-defined wavelength scale. For example, guidelines and restrictions on exposure levels average over predetermined spatial regions, typically [14] $1\,\mathrm{cm}^2$ or $4\,\mathrm{cm}^2$. Isolation hinders
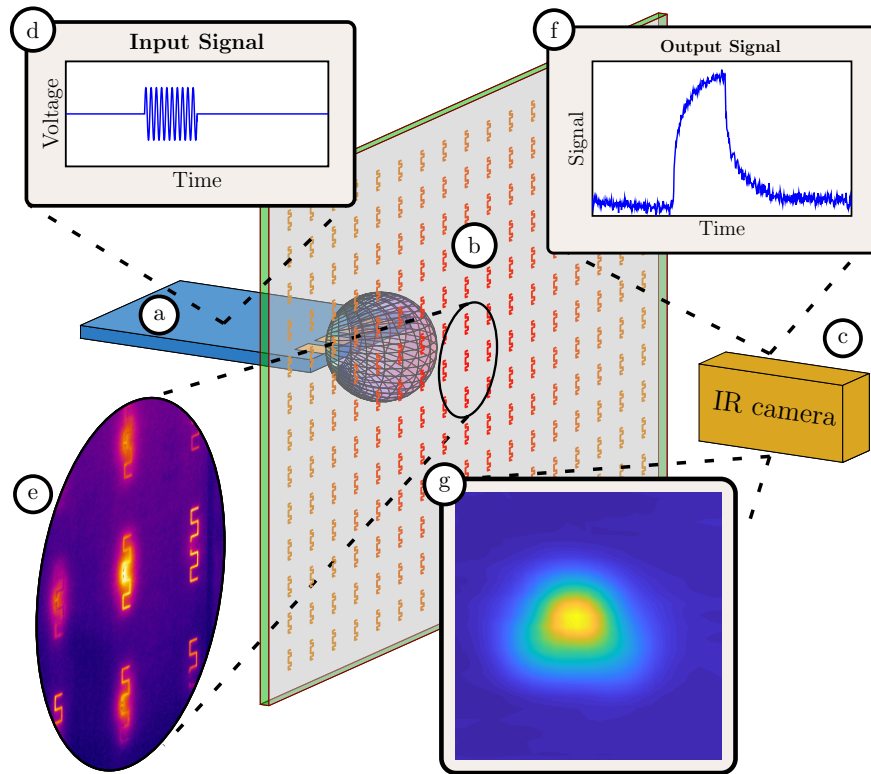
Figure 1: An illustration of a measurement using the metasurface sensor composed of an array of a radiating device (a), thermally isolated elements (b), IR camera (c), the input signal (d), IR image of the metasurface (e), temporal evolution (f), and the resulting image of the field (g).

diffusion of thermal energy and stops blurring of the image, and is achieved by physically separating the sensor metal elements on a substrate with low thermal conductivity.

To address these challenges, and produce images of the electromagnetic field in real-time, we present a metasurface sensor. The electromagnetic response and thermal properties of the metasurface enable an observable temperature increase in localized regions for power density levels below $0.1\,\mathrm{mW/cm^2} = 1\,\mathrm{W/m^2}$. This stands in contrast to generating a temperature increase over the entire sheet [3, 6, 22] or patches [16], which use high power density levels, 27-220 mW/cm^2 for frequencies in the 2-20 GHz range [9, 17, 19, 20]. Important power density levels are generally lower than this and determined by guidelines and restrictions. The ICNIRP [14] states that for frequencies between 6 GHz and 300 GHz, a power density of $1\,\mathrm{mW/cm^2}$ is a low-end limit with a high-end limit of $40\,\mathrm{mW/cm^2}$.

Apart from the geometry, and thermal properties, of the metasurface, the impact of thermal diffusion can be suppressed in the end image by modulating the signal of the radiating device [3]. The structure and a use case is displayed in Fig. 1. A radiating device (a) is placed near the metasurface sensor (b) and in front of the infrared camera (c). The radiating device transmits a signal (d). The radiation impinges on the sensor which absorbs part of the energy and becomes warmer, seen by the infrared image (e). The camera detects the heating and generates an output signal (f) used to retrieve information of the electromagnetic field (g). We have constructed a measurement system for mm-wave radiation based on the metasurface principle outlined above. A manufactured metasurface is measured in this work, and the absorption of energy in small isolated regions shows the possibility of measuring the low power levels from consumer devices. In this letter, electromagnetic radiation refers to the fields radiated by the device, even though infrared radiation also is electromagnetic.

The rest of the paper go through the technique in more detail. The next two section cover the metasurface sensor and input/output signals. Measurement results of a small device are presented before concluding the work. Even though infrared radiation is electromagnetic radiation our mention is strictly for the fields radiated by the device.

2   Metasurface Principle

At the heart of the technique is a metasurface sensor [1, 13, 24], a two-dimensional metamaterial [7, 8]. The purpose is to convert electromagnetic radiation to detectable infrared photons [3, 6, 11, 16, 17, 19, 20, 21, 22, 23]. A high number of photons should correspond to a strong incident electromagnetic field, where we assume that the metasurface is placed outside the reactive near field of the radiating device. Being capable of measuring low power levels requires careful consideration of many physical phenomena. For this, the surface needs to have certain thermal and electromagnetic properties.

The heat should stay localized and not spread over the surface significantly, as this will lower the temperature and blur the image. Our solution is a metasurface with thermally isolated elements on a substrate with low thermal conductivity and low specific heat capacity[4], see Fig. 1. To maximize the interaction and tunability within a certain given frequency interval—that of the radiating device, Fig. 1 (a)—we constructed resonant
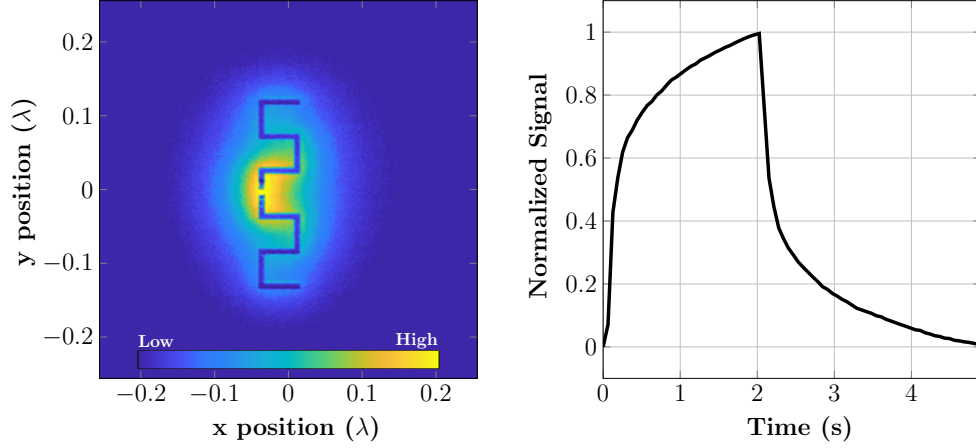
Figure 2: Measured temperature distribution over the element at peak temperature (left) and normalized temperature increase in the resistive element over time (right).

antenna elements [16]. Each antenna element is loaded with a resistor which absorbs the energy and converts it to heat. In specific applications such as near-field measurements, reflection back to the radiating device is unwanted. In these cases the value of the load can be altered to reduce reflection, but also absorption, in effect making the metasurface invisible for the device [5]. Absorption, reflectance, and transmittance of a thin metasurface can be tuned between the peak absorption, 50%, (25% reflectance and transmittance) and lower absorption with either high or low reflectance and transmittance by tuning the load. This is the general principle of the metasurface, of which we present one implementation, see SI.

One element corresponds to one pixel in this mm-wave imaging system. To place the elements close to each other, *i.e.* mimicking a homogeneous metasurface for the radiated field, we design miniaturized antennas. A well-designed resonant element will, in principle, interact with a surrounding region approximately of size λ^2, with λ denoting the wavelength [25]. Many choices on designs exist and in this work we explore meander line antennas, as seen in Fig. 1, a traditional design for small resonant antennas [10].

When interacting with the field, a current passes through the element and, with a resistor in the current's path, heat will be generated through ohmic losses. From this heat, infrared photons are created and must be emitted to be detected. An important parameter of the element is thus the emissivity, which describes how effective a material is in emitting thermal radiation [12]. Metal has low emissivity (high reflectance), and will in this setting appear to have a constant temperature even though the actual temperature has changed [12]. This is demonstrated in Fig. 1 (e), in which the meander lines are visible, although they have the same temperature as the surrounding sheet. The resistors used in this work were prefabricated off-the-shelf-components soldered into place by hand. They were placed in the center of the meander lines where the current is the largest. The main part of the resistor consists of a ceramic material and chromium, which has high emissivity. This yields more infrared photons to detect, and thus a higher signal-to-noise ratio in the infrared camera.

3 Metasurface response

If a device radiates a single frequency continuously, the metasurface will heat up and eventually reach thermal equilibrium depending on the strength of the electromagnetic field. However, obtaining thermal equilibrium in each spatial measurement point and translating it to a power density is complicated and time-consuming [22]. Another way to measure is lock-in thermography [3] or modulate the transmit signal in other ways [16]. Examples include sinusoidal modulation and on/off modulation. Modulation has the benefit of reducing the impact of thermal convection and conduction at a signal-to-noise ratio cost [2]. With a low enough duty cycle of the input signal to allow for cooling back towards the initial state, then the temperature increase, and consequently photon generation, for one period of on/off modulation will approximately follow

$$T(t) \propto \begin{cases} 1 - e^{-t/\tau_r} & 0 < t \le t_0 \\ e^{-(t-t_0)/\tau_f}\left(1 - e^{-t_0/\tau_r}\right) & t > t_0 \end{cases} \tag{3.1}$$

Here, $\tau_{r,f}$ are the characteristic times of the system and the signal is on from $t = 0$ to $t = t_0$. The resulting output signal of a measurement with a transmitting signal, on for two seconds and off for three seconds, is displayed in the right graph of Fig. 2. The curve is well described by the approximate solution to the heat equation described by (3.1).

The spatial distribution of the temperature from a measurement over one element is seen in Fig. 2 and is directly proportional to the absolute square of the incident electric field in the element's principal direction. The temperature increase is confined to the center of the meander line where the resistor is placed. A typical measurement and the regions of interest is displayed in Fig. 3. The main region of interest, acquisition region, is the area surrounding the resistor, here labeled region A. At a first pass, we can investigate the maximal temporal peak temperature of the element compared to the lowest temporal value of the same region. Evident from Fig. 3, the temperature does not spread symmetrically, and the acquisition region is chosen to include most of the thermal energy. A measurement of the mean value of the temperature of region A is seen in the top left (the signal-to-noise ratio is higher in the image than in the graphs to show the spread of thermal energy across the metasurface). The measurement was conducted over three periods, not easily identifiable in this data. This can partly be explained by a change in temperature, due to the camera, ventilation, and other factors. By defining a reference region, region B in Fig. 3, this impact is reduced. In this work, we used a region along the symmetry axis of the element. Provided that an outside factor is affecting both region A and B, it can be compensated for by taking the difference between the signals. The further away the regions are, the less the desired signal in A is leaking into B. Therefore region B is placed close to the edge of the periodic cell in order to increase the signal strength. The mean temperature in region B is shown in the bottom left graph. The output signal, right graph in Fig. 3, obtained by subtracting the temperature of the reference region from the acquisition region, show three clear periods.

The scaling of the received signal strength for varying incident power density levels is seen in Fig. 4. The acquisition region was similar to Fig. 3. The blue lines in Fig. 4 use reference subtracted peak temperature of the acquisition regions. The red lines use the reference subtracted mean temperature of the acquisition region and are less sensitive to
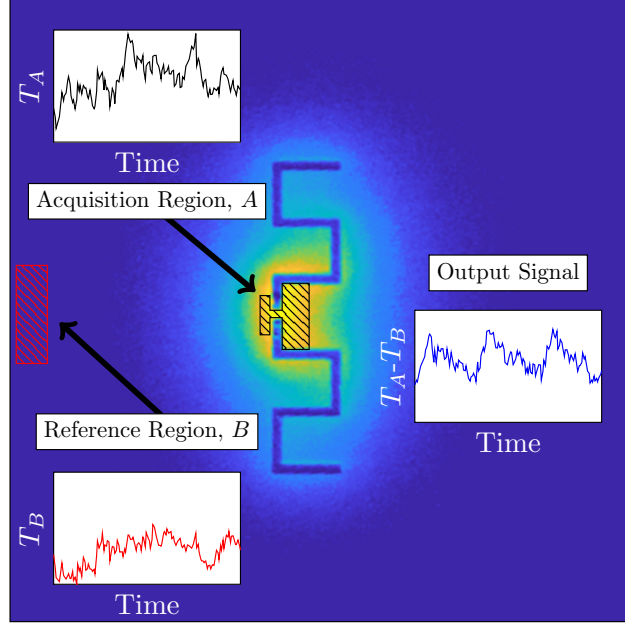
Figure 3: Regions of interest in the signal retrieval shown at peak temperature and the signals in acquisition region *A*, reference region *B*, and output signal.

noise. The dashed lines show a measurement of two periods and the solid lines include around 30 periods for power densities lower than $0.1\,\mathrm{mW/cm^2}$ and around 15 periods for power densities higher than $0.1\,\mathrm{mW/cm^2}$. In an ideal setting the measured temperature, T_{obs}, is directly proportional to the incident power density, P, that is, $T_{\mathrm{obs}} = \alpha P$, where α is a constant. However, noise impacts the system and the equation is better estimated by $T_{\mathrm{obs}} = \alpha P + n$, where n is the noise level. At around 0.05-$0.1\,\mathrm{mW/cm^2}$ the red and blue curves changes shape due to the impact of noise in the experimental setup. With more periods, noise affects the system less, and lower power levels can be measured.

From the physics we expect the approximate response (3.1) to hold. The measured data can be estimated to be on this form, using input parameters as amplitude, characteristic rise, and fall time into simple minimization techniques. With the reference subtracted mean temperature of the acquisition region, and fitting this to an expression on the form of (3.1), we obtain the black solid curve of Fig. 4. There is a linear trend throughout the measurement range and the results show that the constructed metasurface can measure power levels below $0.1\,\mathrm{mW/cm^2}$. Consequently, lower power levels can be observed with this process and form the basis of the on/off measurements in this letter. For any non-pulsed measurements, the reference subtracted mean temperature of the acquisition region was used. Thermal noise, in the non-cooled camera, can be seen to impact the system at low power density levels.

Another aspect of the measuring technique is converting from the measured temperature to a power density level. There are several approaches to calibration. In this work, we used an open-ended waveguide and a calibrated signal generator to extract a value of the incident field from the amplitude of the signal. In Fig. 4 the peak temperature for different values of input power is plotted using a periodic input signal. Fig. 4 converts the measured
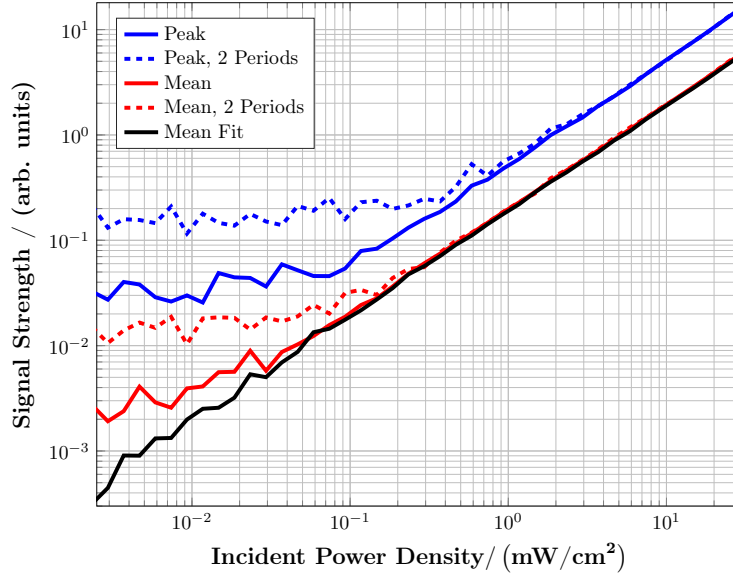
Figure 4: Signal strength in the output data for varying incident power densities for on/off modulation using the peak (blue), and the mean (red) temperature, for two periods (dashed) and around 30 periods for low power densities and around 15 periods for high power densities (solid). In the black line, the output data has been fitted to the form of (3.1).

signal to power density and could serve as calibration.

4   Measurement of a Device

A metasurface consisting of a 3×3 array was constructed for $10 - 13\,\text{GHz}$ and used to measure the field distribution close to a small radiating device (a patch antenna). The metasurface and device are shown in the leftmost column of Fig. 5. The meander line is $0.2\,\text{mm}$ wide and can be confined in a rectangle of dimensions $6.52 \times 1.38\,\text{mm}^2$, see SI. In the image one can see meander like shapes in between the array elements. These are burn marks, a byproduct of the manufacturing, and are not made of metal. The measurements were conducted at $12.25\,\text{GHz}$ to enable the early prototype to be constructed partially by hand. The radiating device was chosen to have a significant cross-polarization component, and we measured close to the radiating device to capture interesting patterns and investigate a region where measurements are non-trivial.

The radiating device was measured in a plane parallel to the patch $5\,\text{mm}$ ($\lambda/5$) away in two ways. In one setting the metasurface was swept continuously over the device and the device radiated a time-harmonic signal. In the center column of Fig. 5 the resulting images are seen for both the co-polarized (y) and cross-polarized (x) components. The co-polarized measurement used an input power of $6\,\text{mW}$ and the cross-polarized used $60\,\text{mW}$. The purpose of these two images is to show the radiated field pattern. In a patch antenna, one expects the fields to be strong near the edges of the patch. This is most obvious in the cross-polarization where two peaks are visible, and situated on each respective edge
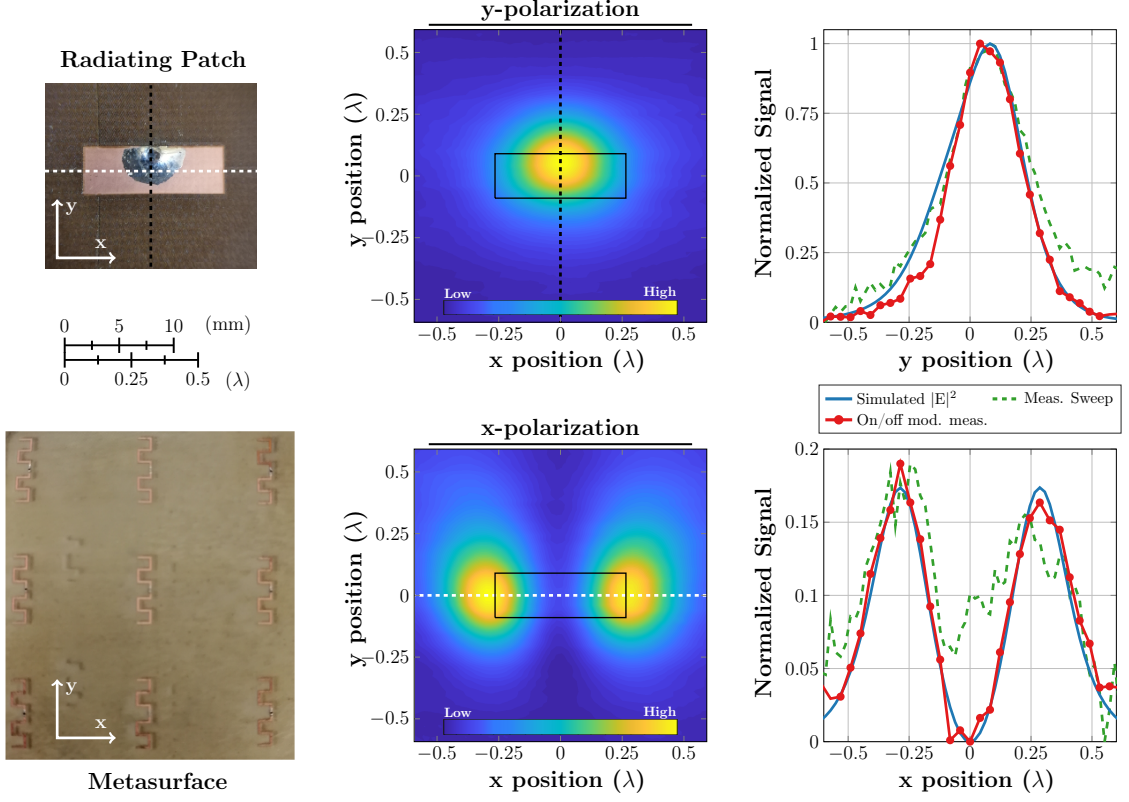
Figure 5: The metasurface and radiating patch, dimensions $12.9 \times 4.5\,\text{mm}^2$, to scale (left column). Field distribution obtained from a continuous scan in a plane 5 mm away from the radiating device in both y (cross) and y (co) polarization with the outline of the patch in solid black (center column). The output signal along the dashed lines for on/off modulation, continuous sweep, and simulation (right column).

of the patch, Fig. 5 bottom center. Similarly, we expect the field in co-polarization to be strong at the feed position and the edge close to it. The feed is placed near the top edge which is where the field is strongest, top row, center, Fig. 5.

To examine the results further, we plot cuts along the x and y directions over the center of the device, see dashed green curves in the rightmost column of Fig. 5. For the measurements generating the rightmost column, a constant input power of 0.6 mW was used, translating roughly to a power density of 0.05-0.5 mW/cm^2 for the cross-polarization and co-polarization measurements. Therefore, the signal is noticeably noisier than in the center column. A second measurement is added in this figure and consisted of 12 periods on/off modulation (on two seconds, off three seconds) per measurement position and fitting the data to an exponential estimate (3.1) as described previously, see solid red curves with markers. Simulations of the patch using the software FEKO are shown in solid blue. The element on the metasurface was of comparable dimensions to the radiating device, yet we observe curves similar to the simulations. In particular for the on/off modulated signal where the technique could capture the sub-wavelength detail of a zero value of the field in the center of the patch in cross polarization, $x = 0$ bottom right Fig. 5.

5 Discussion and conclusion

Using heat to image electromagnetic fields, as done in this letter, using a metasurface for mm-waves, is an interesting concept which combines several physical phenomena. There are many parameters to consider in construction, design, and measurement technique. The design and material might differ for different frequencies, but our focus is on presenting the technique. Although many parameters are at play, the metasurface can be tailored to specific measurement needs such as element positioning, orientation, and reflection back onto the radiating device. The metasurface is flexible and enables real-time measurements of devices without complex measurement environments such as anechoic chambers.

In this work, a technique to measure electromagnetic fields from a mm-wave device through a metasurface and an IR camera is presented. An impinging wave interacts with the surface that dissipates energy through ohmic losses, detected by an IR camera. The concept of the metasurface and a concrete design is presented. A metasurface was manufactured and used to measure a device radiating at $12.25\,\text{GHz}$ in a plane $\lambda/5$ away. The results compare well with simulations of the field and the device could detect very low power levels, less than $0.1\,\text{mW/cm}^2$, compared to previous measurements in the range of 27-220 mW/cm^2 for frequencies in the 2-20 GHz range [9, 17, 19, 20].

This mm-Wave technique is enabled by the rapid, and ongoing, development of thermal cameras in combination with higher frequency electromagnetic waves in everyday scenarios. The metasurface-IR camera is well suited for mm-Wave devices, with elements having low mass and small physical size, to enable detectable signals on a cm-resolution. The technique is relatively inexpensive and flexible—manufacture a metasurface, place it, and image with an IR camera. The technique shows promise for fast evaluation of radiated fields from everyday devices.

A Mechanisms of heat transfer

The mechanisms of heat transfer in the metasurface can be discussed in the simplified context of a two-dimensional thin sheet with thickness d [12]

$$\frac{\partial u}{\partial t} = \frac{P(t)}{c_{\text{p}}\rho}f(\boldsymbol{r}) + \frac{k}{c_{\text{p}}\rho}\nabla^2 u + \frac{2h}{c_{\text{p}}\rho d}(T_0 - u) + \frac{2\varepsilon\sigma}{c_{\text{p}}\rho d}(T_0^4 - u^4) \qquad \text{(A.1)}$$

where $u(\boldsymbol{r}, t)$ is the temperature in the sheet at position $\boldsymbol{r} = (x, y)$ and time t. Heat is supplied by the device under test (DUT) with total radiated power $P(t)$, where the time dependence is due to power modulation of the DUT. The resulting spatial distribution of ohmic heat in the metasurface at unit output power of the DUT is denoted $f(\boldsymbol{r})$. The specific heat capacity at constant pressure is denoted c_{p}, and the density is ρ. The heat is

dissipated in the form of diffusion, convection, and radiation, represented by the last three terms in (A.1). The factor k is the thermal conductivity, h is the convective heat transfer coefficient, ε is the emissivity of the object, σ is Stefan-Boltzmann's constant, and T_0 is the background temperature [12]. The radiation term corresponds to the photons that we observe with the IR camera and can be linearized to $\frac{\varepsilon\sigma}{c_p\rho d}8T_0^3(T_0-u)$ for small temperature differences. The factor of 2 in the convective and radiative terms is due to the two sides of the sheet.

We aim for a design where the ohmic losses are concentrated to a small resistive part of the element, see Fig. 2, where it is desirable to dissipate as much as possible through radiation. Thus, we want to minimize the diffusion in the substrate (small k), and the convective losses (small h), while maximizing the IR-radiation from the resistor (large ε). Whereas k is available in many orders of magnitude, h is typically around $5\,\mathrm{W}/(\mathrm{m}^2\mathrm{K})$ for a smooth planar surface surrounded by air, and higher if the surface is textured.[26] At room temperature ($T_0 \approx 293\,\mathrm{K}$), the heat transfer coefficient due to radiation is proportional to $\sigma 4T_0^3 = 5.7\,\mathrm{W}/(\mathrm{m}^2\mathrm{K})$, and is maximized by using materials with high emissivity ε.

Solving (A.1) for a metasurface requires discretization of a non-trivial geometry with several materials involved, feasible with numerical solvers, for instance, based on the finite element method [12]. For a successful design, where diffusion processes can be ignored, this is an ordinary differential equation in time that can be solved for a given excitation $P(t)$. A typical scenario may be where the DUT is on for some time t_0 and is then turned off. The solution is then composed of simple exponentials,

$$u(t) \propto \begin{cases} 1 - \mathrm{e}^{-t/\tau} & 0 < t \le t_0 \\ \mathrm{e}^{-(t-t_0)/\tau}\left(1 - \mathrm{e}^{-t_0/\tau}\right) & t > t_0 \end{cases} \tag{A.2}$$

The characteristic time is $\tau = c_p\rho d/(2h + \varepsilon\sigma 8T_0^3)$. When taking diffusion and more accurate three-dimensional modeling into account, no such simple expression is possible. In this case, (A.1) is changed by letting $\boldsymbol{r} = (x, y, z)$ be a full three-dimensional position vector, and the convection and radiation terms in (A.1) are instead included in the boundary conditions. This approach is used for the detailed simulations in Sec. C. However, (A.2) can be improved by separating the characteristic time in rise and fall region to account for the different physical processes involved in the full model [9]. This modifies (A.2) to yield (3.1).

B   Metasurface elements

The metasurface consists of several elements, each with a region where heat can be generated, in an array fashion, see Figs. 1 and 5. Each element can be considered a measurement point in conventional probe scanning setups, which in this configuration can all be evaluated simultaneously. The temperature increase in the element is larger if the element is constructed with less material, as the absorbed energy is used to heat a region of smaller mass. The element can be designed in several ways and this section presents two designs, see Fig. 6, used in this work and suitable material properties of the different components.
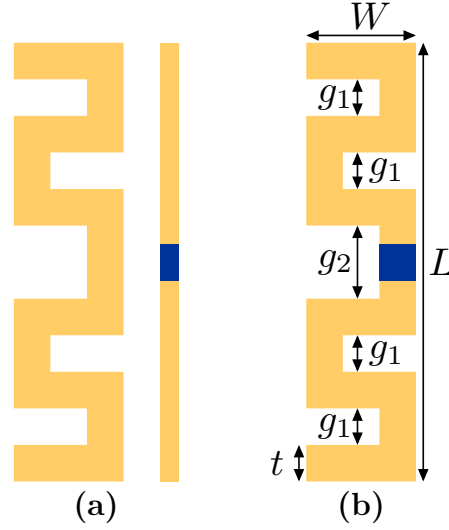
Figure 6: Example designs of meta elements: (a) capacitively coupled meander line and (b) meander line. The gold-colored material is the electrically conducting material, and the blue-colored material is the resistor.

The heat spreads rapidly across the gold-colored regions depicted in Fig. 6 as the material candidate of this region is metal, which inherently conducts heat well, see also Fig. 2. In order to confine the heating to a region of lesser mass, and thus possibly resulting in a higher temperature increase, a design of capacitively coupled regions in Fig. 6 (a) may be utilized, see also Sec. E.

The geometrical parameters of the designs differ depending on the frequency used, material choice, and periodicity of the elements. The chosen design depends heavily on the parameters and fabrication. As long as the skin depth is not compromised, the thickness of the element matters little for the electromagnetic properties but is very important in order to reduce mass. The materials considered in this work are primarily copper, gold, and silver as candidates for the conducting region, and for the resistive part, we have considered prefabricated resistors and alloys such as NiCr of varying compositions. Further investigations into physical and geometrical parameters are done in the following sections covering parameter studies of material parameters and optimization of the geometry.

The elements should be constructed to be resonant to the incoming electromagnetic wave, as this will increase the effective area and provide a high interaction with the electromagnetic field [5, 25] as well as tunability.

Considering the metasurface to be thin and modeling it as a resistive sheet with resistance R, we obtain the relation between reflectance and absorptance for a general resistive sheet as [5]

$$\mathcal{R} = \frac{1}{(2R/\eta_\mathrm{T} + 1)^2} \quad \text{and} \quad \mathcal{A} = \frac{4R/\eta_\mathrm{T}}{(2R/\eta_\mathrm{T} + 1)^2}, \tag{B.1}$$

where η_T is the transverse wave impedance. These relations are illustrated in Fig. 7 for normal incidence with $\eta_\mathrm{T} = \eta_0$, where η_0 is the wave impedance of free space. The transmittance $\mathcal{T}$ is obtained from power conservation, $\mathcal{R} + \mathcal{A} + \mathcal{T} = 1$. The maximal
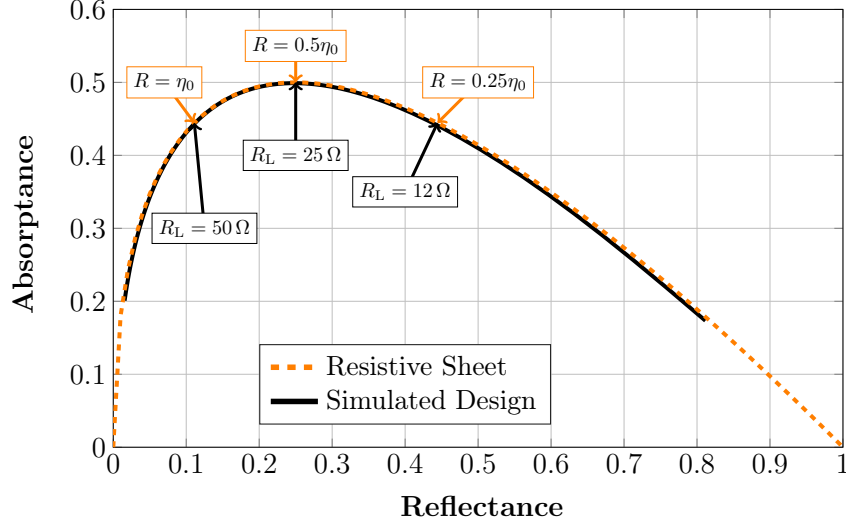
Figure 7: Relationship between reflectance and absorptance for a resistive sheet (B.1), dashed, and simulated design, solid. The solid curve was generated by changing the load resistance, R_{L}, of a tuned design.

absorptance is 50 % at which the reflectance is 25 % and the transmittance is 25 %.

The software used to simulate the physics and optimize the design was COMSOL, in combination with MATLAB. A planar periodic model was constructed, including the physics, of which the simplified version was presented in Sec. A, and simulated on an i7-7700 machine. During the optimization process it is important to optimize the designs based on the end goal of detecting temperature increase with an IR camera. Increasing the average temperature in the load resistor is not enough, but rather the signal of the receiving device should be considered. Both geometrical and physical parameters were investigated during the optimization process, in which the average temperature in the acquisition region in relation to the reference region was maximized, see Fig. 3 in the main letter.

The manufactured design, used for the measurements in the letter, consisted of a meanderline as illustrated in Fig. 6 (b) of thickness $t = 0.2\,\mathrm{mm}$, length $L = 6.52\,\mathrm{mm}$, width $W = 1.38\,\mathrm{mm}$, and gaps $g_1 = 0.98\,\mathrm{mm}$ and $g_2 = 1.38\,\mathrm{mm}$. The sheet consisted of XT-duroid 8100 and the metal part of the elements was $18\,\mu\mathrm{m}$ thick copper and the resistors were thick film resistors from Yageo. As described in Sec. B the load can be changed to adjust the reflectance and transmittance tradeoff. Using a well-optimized design and changing the load will shift the design along the resistive sheet approximation. This is seen by the solid line in Fig. 7. With a well-designed element, the load resistance may be chosen to fit the specific needs of the measurement system.

C   Substrate and materials

The simulations presented are for an already optimized design and the impact of parameters, as presented in Fig. 8, is for this specific case. However, the general trend of parameter values and impact of different terms in the main letter remains for different
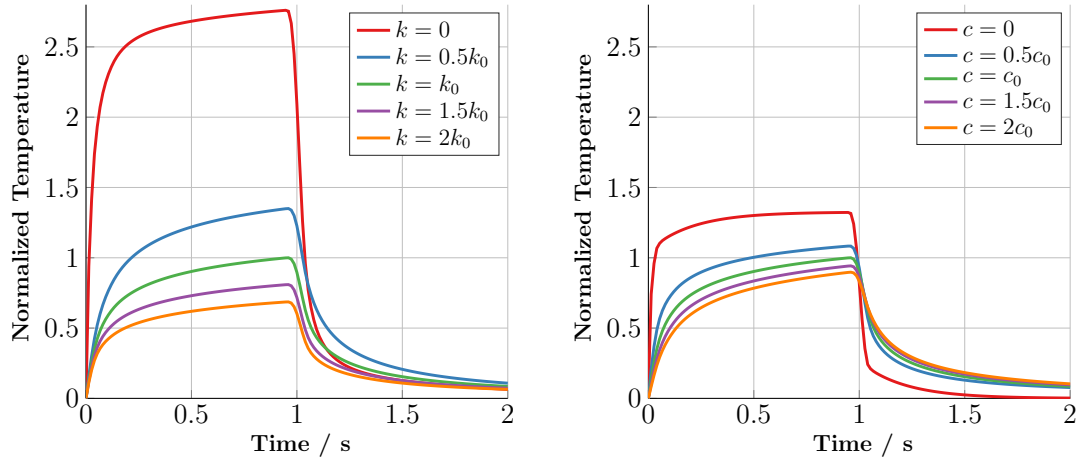
Figure 8: Temperature increase in the resistive element over time for different values of thermal conductivity (left) / specific heat capacity (right) in the sheet normalized to the PTFE laminate XT-duroid 8100 labeled k_0 and c_0.

designs. The thermal parameters of the resistor were also investigated. For this particular design, consisting of a very thin layer, 10 nm, of resistive material situated on a 50 μm substrate, the impact of the thermal properties of the resistor was not noticeable. For a resistor of more mass, it might differ. The important parameter of the resistor is the resistance, as seen in Fig. 7. Suitable material candidates are gold/silver etc for the meander line segment of the element and the resistive region could be NiCr, see Fig. 6.

Heat conduction in the substrate as well as convection in the air are important factors and have a large impact on an otherwise functioning design, see Sec. A. There is little to be done regarding the convection of the surrounding air. However, the substrate can be chosen freely. From the bottom graph of Fig. 8 we can see how the average temperature in the resistor is affected by changing the specific heat capacity, c_p and the thermal conductivity k of the sheet, see (A.1). The parameters are normalized to that of the polytetrafluoroethylene (PTFE) sheet, labeled k_0 and c_0. From these two figures, it is seen that the sheet should have low thermal conductivity and heat capacity. Reducing the heat conduction in the sheet also reduces the impact of convection. Good candidates for substrates are PTFE based laminates such as Rogers XT-duroid 8100, $c_p \approx 1000 \, \text{W/kg}$, $\rho = 1.6 \cdot 10^3 \, \text{kg/m}^3$, and $k = 0.3 \, \text{W/(m K)}$, or Rohacell 51, $c_p \approx 2400 \, \text{W/kg}$, $\rho \approx 75 \, \text{kg/m}^3$ and $k = 0.036 \, \text{W/(m K)}$. PTFE can be utilized in a very thin sheet and rohacell is a porous material in sheets of thicknesses often 1 mm and larger, and as such they pose different challenges in manufacturing.

D   Setup and Measurements

The measurements were done on in-house fabricated designs of types seen in Fig. 6. They were manufactured to operate at frequencies between 10 and 13 GHz.

For the power density measurements yielding Fig. 4, a waveguide and a calibrated signal generator were used. A single element was measured and the DUT was an open-

ended waveguide which the element was placed in front of. The element was illuminated by a uniform incident power density polarized in the direction of the element, provided by the waveguide. The illuminating waveguide was connected to a signal generator providing power density levels between 0–13 mW/cm^2. The output power was confirmed by a power measurement with a calibrated VNA as well as a power meter. The waveguide was used due to its simple and robust radiation pattern. The elements were placed in front of the waveguide and the signal was swept over frequency and amplitude. The data presented in Fig. 4 is for the resonance frequency.

The measurements used to generate Fig. 5 consisted of mounting a 3×3 metasurface a fixed distance from a FLIR A655sc camera. The position of the metasurface and IR camera was controlled by two positioners, enabling a scan in a 30×30 cm^2 plane. For the continuous signal measurement, *i.e.*, the 2D plots and green dashed curves in Fig. 5, the mean temperature over a region of the resistor was logged as the positioners scanned. For the on/off modulated measurements, *i.e.*, the red solid curves with markers in Fig 5, the signal was on for two seconds, off for three seconds, and 12 periods were measured for each point. The data was fitted to the estimate (3.1) and measured using the output power of 1 mW on the signal generator. Accounting for matching and cable losses etc, -1.2 dB, this yielded an input power of 0.6 mW roughly translating to a power density of 0.05-0.5 mW/cm^2 for the cross-polarization and co-polarization measurements.

E   IR Cameras

The technique was tested using three different IR cameras, in various degrees. These cameras were an entry-level budget handheld device FLIR E6, a non-cooled scientific-grade camera FLIR A655sc, and a cooled scientific-grade camera FLIR A6752sc. Macro lenses were available and utilized for the scientific grade cameras.

The lenses enabled high-resolution imaging of the single element imaged. In Fig. 9, images are shown of the element as viewed from FLIR A655sc and A6752sc where (a) is from FLIR A6752sc with a macro lens, (b) from A655sc with a macro lens, and (c) without.

The region of interest was the center of the top metal strip, in which the resistor was located. The copper is visible in these figures due to the contrast in emissivity to the background sheet. The temperature was recorded for different lengths of time, ranging from around 4 periods up to around 200 periods.

In the simulations, the temperature in the element could be directly computed, but during measurements, it has to be observed through the IR camera. This adds additional difficulty as the camera is situated a short distance away with air continuously flowing in the region between the sheet and sensor. To measure very small temperature changes a reference region, ≈ 1 cm away from the element was defined. The temperature in this region was mostly unaffected by the small temperature increase in the element but contained the temperature changes due to other unwanted effects such as drafts. The raw data was processed by comparing the acquisition region with the reference region for every measured time point. All the measured periods were then combined to create an average temperature increase in the element. The raw data and the processed corrected
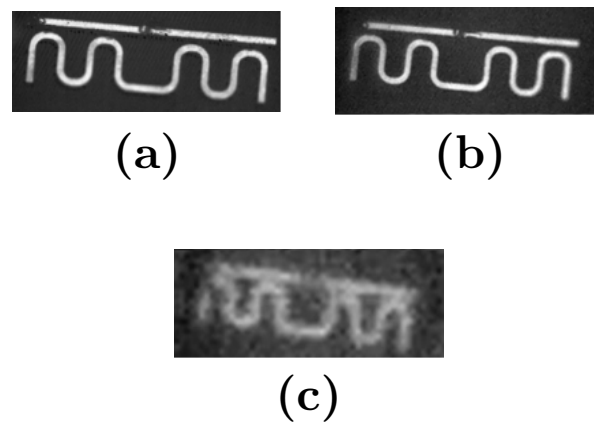
Figure 9: Images of the element as seen by the scientific grade cameras. a) A6752sc with macro lens, b) A655sc with macro lens and c) A655sc without macro lens.

data are visible in Fig. 10. The reference region data is shown in green color and the mean temperature of the acquisition region in orange. The solid red line shows the time-synchronous signal average.

It is immediately clear in Fig. 10 that the non-cooled cameras, column 2-4, experience internal drift in temperature, as the background temperature varies over the measurement time. This is due to the nature of the sensor. The sensors in these cameras are heated by the incoming radiation and consequently, get warmer and are subject to leaking to neighboring pixels. Periodically the camera is recalibrated by letting the pixels get in contact with a reference surface. A measurement setup using these cameras is thus required to have a reference region unless only temperature slope information during very short time intervals is to be extracted. There are also minor changes in the background temperature in the measurement utilizing the cooled camera, FLIR A6752sc. However, this is not on a significant level. Using subtraction of the reference region, the impact of these effects can be reduced and the temperature change is visible. For the non-cooled cameras, longer measurement time seems to be needed. The incident power density was the same for all measurements and an equal temperature increase is expected. The A6752sc and A655sc cameras, with a macro lens, capture a 0.17 degree temperature change in the one-second window when the signal is "on". The shape is agreeable to the curve presented in Fig. 2 in the main letter. The fine details of the heating are lost without the macro lens, and for the A655sc without a macro lens and the handheld E6 device, a temperature difference of 0.1 and 0.03 degrees was observed, respectively. The time-synchronous signal averages for all measurements are seen in Fig. 11.

The curves have been shifted to have the same baseline temperature. There is an observable change detected for all cameras, but a large difference in how easily and rapidly it can be detected. In this work, we are not interested in characterizing the temperature directly, rather the power density of the electromagnetic field, and thus relating the performance of the graphs in Fig. 11 to a specific power density value is a calibration issue. There are also factors of camera settings and emissivity which factor into the absolute numbers of the temperature change.
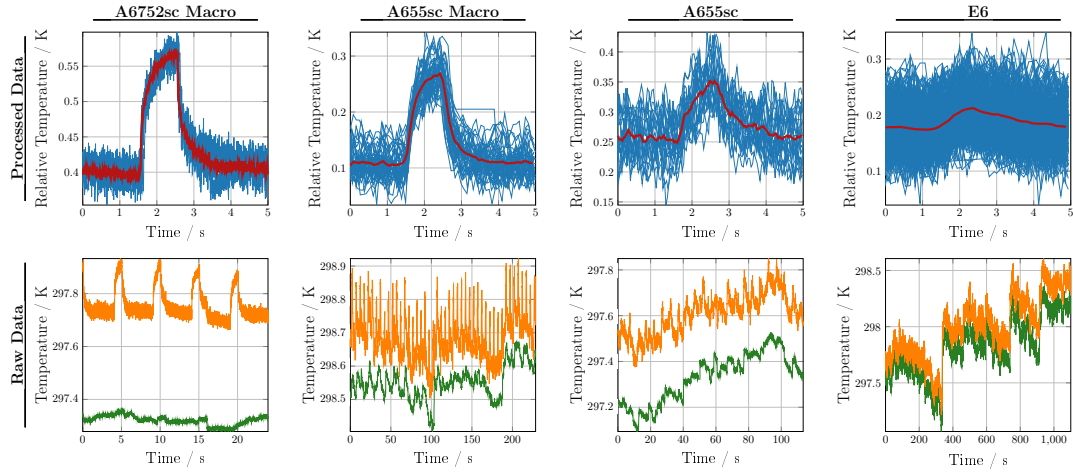
Figure 10: Measurement results of the different cameras and lenses, columns. Processed data is in the top row and raw data on the bottom. The reference data is shown in green color and the temperature of the element in orange, bottom row. The red line shows the time-synchronous signal average, and the blue line is the data gathered within one period.

References

[1] K Achouri and C Caloz. "Electromagnetic Metasurfaces: Theory and Applications". Wiley-IEEE Press, 2021.

[2] D. Balageas and P. Levesque. "EMIR: a photothermal tool for electromagnetic phenomena characterization". *Revue générale de Thermique* 37 (8) (1998): pp. 725–739.

[3] D. L. Balageas, P. Levesque, and A. A. Deom. "Characterization of electromagnetic fields using a lock-in infrared thermographic system". In: *Thermosense XV: An International Conference on Thermal Sensing and Imaging Diagnostic Applications*. Vol. 1933. International Society for Optics and Photonics. 1993, pp. 274–285.

[4] R. B. Bird, W. E. Stewart, and E. N. Lightfoot. "Transport Phenomena". John Wiley & Sons, 2006.

[5] J. G. van Bladel. "Electromagnetic Fields". Second Edition. IEEE Press, 2007.

[6] K. Brown. "Far-field antenna pattern measurement using near-field thermal imaging". *IEEE Trans. Antennas Propag.* 66 (3) (2018): pp. 1488–1496.

[7] F. Capolino, ed. "Metamaterials Handbook". CRC press, 2009.

[8] N. Engheta and R. W. Ziolkowski. "Metamaterials: physics and engineering explorations". John Wiley & Sons, 2006.

[9] K. Fan, J. Y. Suen, X. Liu, and W. J. Padilla. "All-dielectric metasurface absorbers for uncooled terahertz imaging". *Optica* 4 (6) (2017): pp. 601–604.

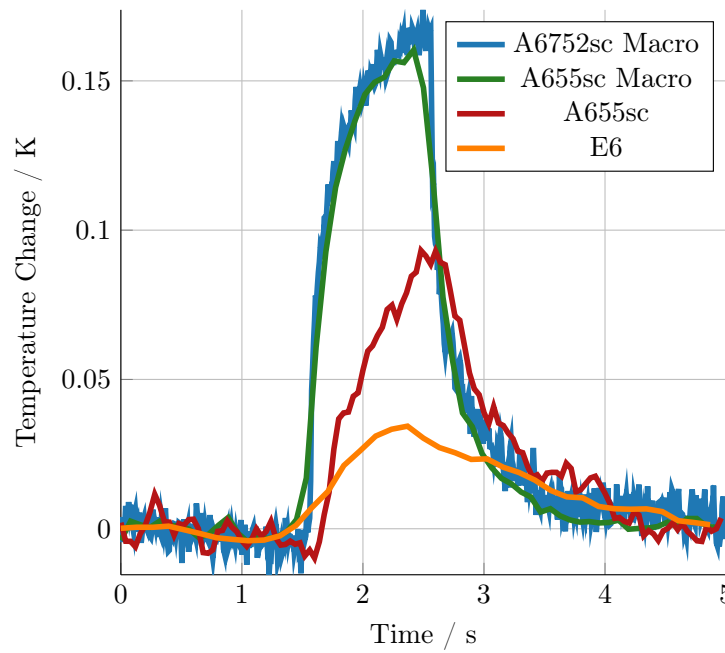[10] K. Fujimoto and H. Morishita. "Modern small antennas". Cambridge University Press, 2013.

Figure 11: Time-synchronous signal average of all four measurements presented in Fig. 10.

[11] L. G. Gregoris and K. Iizuka. "Thermography in microwave holography". *Applied optics* 14 (7) (1975): pp. 1487–1489.

[12] J. R. Howell, M. P. Menguc, and R. Siegel. "Thermal Radiation Heat Transfer". CRC Press, 2010.

[13] H.-H. Hsiao, C. H. Chu, and D. P. Tsai. "Fundamentals and applications of metasurfaces". *Small Methods* 1 (4) (2017): p. 1600064.

[14] International Commission on Non-Ionizing Radiation Protection (ICNIRP). "Guidelines for limiting exposure to electromagnetic fields (100 kHz to 300 GHz)". *Health Phys.* 118 (5) (2020): pp. 483–524.

[15] J. D. Jackson. "Classical Electrodynamics". Third. John Wiley & Sons, 1999.

[16] S. A. Kuznetsov, A. G. Paulish, M. Navarro-Cía, and A. V. Arzhannikov. "Selective pyroelectric detection of millimetre waves using ultra-thin metasurface absorbers". *Scientific reports* 6 (2016): p. 21079.

[17] S. A. Kuznetsov, A. G. Paulish, A. V. Gelfand, P. A. Lazorskiy, and V. N. Fedorinin. "Bolometric THz-to-IR converter for terahertz imaging". *Applied Physics Letters* 99 (2) (2011): p. 023501.

[18] J. Lundgren, M. Gustafsson, D. Sjöberg, and M. Nilsson. "IR and metasurface based mm-wave camera". *Appl. Phys. Lett.* (2021).

[19] K. Muzaffar, K. Chatterjee, L. I. Giri, S. Koul, and S. Tuli. "Modelling and analysis of power distribution of electromagnetic waves on plane surfaces using lock-in IR thermography". *Journal of Nondestructive Evaluation* 36 (3) (2017): p. 60.

[20] K. Muzaffar, L. I. Giri, K. Chatterjee, S. Tuli, and S. Koul. "Fault detection of antenna arrays using infrared thermography". *Infrared Physics & Technology* 71 (2015): pp. 464–468.

[21] K. Muzaffar, S. Tuli, and S. Koul. "Beam width estimation of microwave antennas using lock-in infrared thermography". *Infrared Physics & Technology* 72 (2015): pp. 244–248.

[22] J. Norgard and R. Musselman. "Direct infrared measurements of phased array near-field and far-field antenna patterns". *Quantitative InfraRed Thermography Journal* 2 (1) (2005): pp. 113–126.

[23] D. Prost, F. Issac, and M. Romier. "Imaging electric and magnetic near field of radiating structures by infrared thermography". In: *2019 International Symposium on Electromagnetic Compatibility-EMC EUROPE*. IEEE. 2019, pp. 311–314.

[24] O. Quevedo-Teruel, H. Chen, A. Díaz-Rubio, G. Gok, A. Grbic, G. Minatti, E. Martini, S. Maci, G. V. Eleftheriades, M. Chen, et al. "Roadmap on metasurfaces". *Journal of Optics* 21 (7) (2019): p. 073002.

[25] S. Silver. "Microwave Antenna Theory and Design". Vol. 12. Radiation Laboratory Series. McGraw-Hill, 1949.

[26] J. Welty, G. L. Rorrer, and D. G. Foster. "Fundamentals of momentum, heat, and mass transfer". John Wiley & Sons, 2020.